Terbit *online* pada laman web jurnal : http://metal.ft.unand.ac.id

METAL: Jurnal Sistem Mekanik dan Termal

| ISSN (Print) 2598-1137 | ISSN (Online) 2597-4483 |

Research Article

Mechanical and Failure Characterization of Vacuum-Infused Carbon/Glass/CSM Hybrid Laminates

Ilhamdi [1,], Bagus Fadli Wahyu Stiawan[1], Hendri Hestiawan[2], Dony Hidayat[3]*

[1]*Department of Mechanical Engineering, Universitas Andalas, Padang 25163, Indonesia*
[2]*Department of Mechanical Engineering, Universitas Bengkulu, Bengkulu 38122, Indonesia*
[3]*Aviation Technology Research Center, National Research and Innovation Agency (BRIN), Bogor 16610, Indonesia*

ARTICLE INFORMATION

Article History:
Received: 27 July 2026
Revised: 28 October 2026
Accepted: 30 October 2026

KEYWORDS

Hybrid laminate
Vacuum infusion
Flexural behavior
Failure analysis
Mechanical characterization

CORRESPONDENCE

E-mail: ilhamdi@eng.unand.ac.id

A B S T R A C T

The increasing demand for lightweight structures in unmanned aerial vehicles (UAVs) requires composite materials that balance structural stiffness and damage tolerance. This study experimentally investigates the mechanical performance and macroscopic failure behavior of a vacuum-infused seven-layer Carbon/Glass/CSM hybrid laminate with a [C/G/CSM/C/G/CSM/C] stacking sequence, using monolithic carbon fiber reinforced polymer (CFRP) as the benchmark. Tensile properties were evaluated with reference to ASTM D3039 using adapted dog-bone specimens resembling ASTM D638 Type I, while three-point bending tests followed ASTM D790. The hybrid laminate achieved average tensile and flexural strengths of 395.6 MPa and 294.1 MPa, respectively, compared with 610.6 MPa and 443.9 MPa for CFRP. Its flexural modulus was 32.2 GPa, and its flexural strain at break was comparable to CFRP (approximately 0.8%). Both laminates exhibited predominantly brittle behavior under tensile loading. Under flexural loading, the hybrid laminate showed a progressive post-peak response characterized by sawtooth-shaped stress fluctuations, an extended load plateau, and sustained load-carrying capacity, whereas CFRP exhibited abrupt post-peak failure. Macroscopic observations after unloading showed a visible spring-back response in the hybrid specimens, while CFRP specimens retained permanent bending deformation. The hybrid laminate exhibited carbon fiber fracture, fiber pull-out, fiber bridging, localized edge delamination, and matrix fragmentation. Although hybridization reduced ultimate mechanical strength, the observed flexural response indicates more progressive damage development, suggesting potential for lightweight secondary UAV structures where damage progression is important.

1. INTRODUCTION

The increasing demand for lightweight structural systems in aerospace, transportation, and unmanned aerial vehicle (UAV) applications has accelerated the development of advanced composite materials capable of providing high specific strength, high stiffness, and improved structural reliability [1]. Besides reducing structural weight, composite materials are expected to maintain sufficient load- carrying capability and damage tolerance under tensile and bending loads encountered during service. These requirements are particularly important for lightweight structural components, such as control surfaces, fairings, access panels, and other secondary load-bearing structures, where structural efficiency and

https://doi.org/ 10.25077/metal.10.2.111-123.2026

This is an Open Access article distributed under the terms of the Creative Commons Attribution-NonCommercial-ShareAlike 4.0 International License

manufacturing cost must be considered simultaneously.

Carbon Fiber Reinforced Polymer (CFRP) has become one of the most widely adopted structural composite materials because of its excellent specific mechanical properties and fatigue resistance. However, conventional CFRP laminates generally exhibit linear elastic behavior followed by sudden brittle fracture after reaching the ultimate load, providing little warning before catastrophic failure [2]. Such behavior limits structural damage tolerance and motivates the development of composite systems capable of achieving a more progressive failure process while maintaining satisfactory mechanical performance.

Hybridization has been extensively investigated as an approach to combine the advantages of different reinforcing fibers within a single laminate [3]. Carbon fibers provide high stiffness and tensile strength, whereas fiberglass contributes higher strain capacity and improved energy absorption [4]. The incorporation of chopped strand mat (CSM) may further influence interlaminar stress transfer because of its randomly oriented fiber architecture. Besides laminate architecture, manufacturing quality also plays a significant role in determining composite performance [5]. Vacuum infusion has become an attractive manufacturing process because it enables relatively uniform resin impregnation, reduced void content, and economical fabrication of medium-scale composite structures compared with conventional hand lay-up processes [6].

Although hybrid carbon/glass composites have been widely reported, previous studies have primarily focused on thin-ply or unidirectional laminates designed to achieve pseudo-ductile behavior under controlled laboratory conditions. Experimental investigations on woven Carbon/ Glass/CSM hybrid laminates manufactured by vacuum infusion remain limited, particularly regarding the relationship between tensile properties, flexural properties, and macroscopic failure characteristics under practical fabrication conditions. Understanding these characteristics is essential for assessing the structural capability of hybrid laminates intended for lightweight engineering applications.

Therefore, this study investigates the mechanical properties and macroscopic failure characteristics of vacuum-infused Carbon/Glass/CSM hybrid laminates through tensile testing evaluated with reference to ASTM D3039 using adapted dog-bone specimens resembling ASTM D638 Type I, and three-point bending testing according to ASTM D790.

2. METHODS

2.1. Materials and Stacking Sequence

Two laminate configurations were investigated in this study, consisting of a hybrid carbon/glass/chopped strand mat (CSM) laminate and a monolithic Carbon Fiber Reinforced Polymer (CFRP) laminate used as the benchmark. The hybrid laminate was fabricated using bidirectional carbon fiber with a 2/2 twill weave architecture 240 grams per square meter (gsm) or g/m^2, bidirectional fiberglass with a plain weave architecture (200 gsm), and fiberglass chopped strand mat (CSM) with random fiber orientation (200 gsm). An epoxy thermoset resin and its corresponding hardener were used as the matrix system because of their compatibility with the vacuum infusion process and their good interfacial adhesion with carbon and glass fiber reinforcements.

The hybrid laminate was manufactured using a seven-layer stacking sequence of Carbon/Glass/CSM/Carbon/Glass/CSM/Carbon (C/G/CSM/C/G/CSM/C). For comparison, the benchmark laminate consisted of seven layers of bidirectional carbon twill weave (240 gsm) fabricated under the same processing conditions. Both laminate configurations were prepared by sequentially arranging the reinforcement layers on the mold prior to vacuum infusion. The laminate stacking sequences and the vacuum infusion setup are illustrated in Figure 1.

 https://doi.org/ 10.25077/metal.10.2.111-123.2026

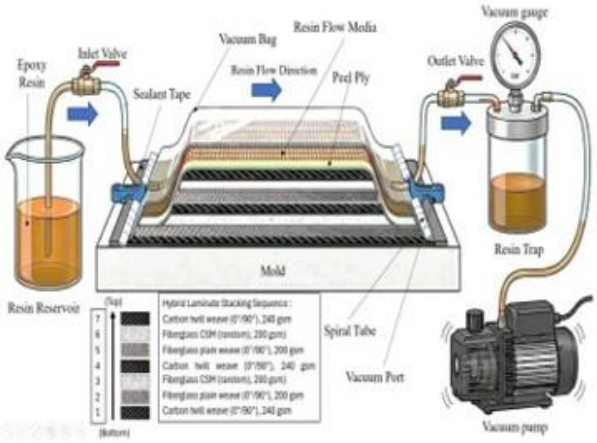


Figure 1. The laminate stacking sequences and the vacuum infusion setup

2.2. Laminate Fabrication

The hybrid and CFRP laminates were fabricated at the RDP Carbon Workshop, Bogor, using the Vacuum Infusion (VI) process. This manufacturing method was selected because it provides improved resin impregnation and laminate quality compared with conventional hand lay-up processes [2]. Prior to fabrication, the mold surface was cleaned and coated with a release agent. The reinforcement layers were subsequently arranged according to the designated stacking sequence described in Section 2.1, followed by the installation of peel ply, flow media, spiral tube, vacuum bagging film, and sealant tape to establish the vacuum infusion system.

After the vacuum system had been assembled, a leak check was performed before resin infusion. The epoxy resin and hardener were mixed according to the manufacturer's recommended ratio and infused into the laminate under vacuum until complete fiber impregnation was achieved [7]. The laminates were then cured under ambient workshop conditions before being removed from the mold and trimmed into the required specimen dimensions for subsequent mechanical testing.

2.3 Specimen Preparation

Following room-temperature curing, the composite laminates were removed from the mold and cut into test specimens using the cutting equipment available at the workshop. The specimen edges were subsequently finished using fine-grit sandpaper to minimize edge irregularities that could induce premature failure during mechanical testing.

The tensile specimens were prepared using a dog-bone geometry resembling ASTM D638 Type I. This geometry was adopted as a practical adaptation considering the available workshop fabrication and cutting facilities. It was intended to reduce the likelihood of premature failure in the gripping region when testing woven composite laminates without dedicated end tabs. However, this configuration differs from the specimen geometry generally used for tensile testing of fiber-reinforced polymer laminates under ASTM D3039. Accordingly, the specimens are described as adapted dog-bone specimens rather than standard ASTM D3039 specimens. Their geometry and nominal dimensions are illustrated in Figure 2. The tensile tests and data evaluation were performed in accordance with ASTM D3039, which is specifically intended for fiber-reinforced polymer laminates [8]. It is important to note that while this dog-bone geometry was selected to reduce the likelihood of premature grip-related failure. It introduces localized stress concentrations at the fillet radius [9].

Consequently, the reported ultimate tensile strengths should be interpreted as apparent (or effective) strengths for this specific geometry, rather than absolute intrinsic material properties. Nevertheless, because the elastic modulus was derived exclusively from the linear-elastic slope within the uniform, parallel central section of the gauge.

Additionally, due to the high sensitivity of the UTM's load cell, the machine-reported fracture strains were triggered prematurely. Therefore, the apparent fracture strains presented in this study were manually recalculated based on post-test displacement measurements to serve as the final strain data.

The flexural specimens were prepared as rectangular specimens according to ASTM D790 for three-point bending testing. Five specimens were prepared for each laminate configuration for

both tensile and flexural tests. The dimensions of all specimens were measured using a digital vernier caliper before testing.

2.4 Mechanical Testing

Mechanical characterization was performed at the Aerostructure Laboratory, National Research and Innovation Agency (BRIN), Bogor, using a Universal Testing Machine (UTM) (TENSILON RTF-2410, A&D Co., Japan) equipped with a 100 kN load cell. Five specimens were tested for each laminate configuration to evaluate the tensile and flexural properties of the hybrid and benchmark CFRP laminates.

2.4.1 Tensile Test

The tensile properties were evaluated with reference to ASTM D3039, which is intended for fiber-reinforced polymer composite laminates. The tests were performed under displacement-controlled loading at a constant crosshead speed of 5 mm/min. The adapted dog-bone specimens had a reduced parallel-section length of 57 mm. Five specimens were tested for each laminate configuration. Load and displacement were continuously recorded by the machine data acquisition system until specimen failure.

The tensile stress (σ) was calculated as:

$$\sigma = \frac{P}{A} \quad (1)$$

where P is the applied tensile load (in Newtons) and A is the cross-sectional area of the gauge section (in mm²). The tensile strain (ε) was calculated from the recorded displacement relative to the gauge length (L_0) using:

$$\varepsilon = \frac{\Delta L}{L_0} \quad (2)$$

where ΔL is the measured displacement. The elastic modulus (E) was determined from the slope of the linear elastic region of the stress-strain curve within the central parallel section, calculated as:

$$E = \frac{\Delta\sigma}{\Delta\varepsilon} \quad (3)$$

where $\Delta\sigma$ and $\Delta\varepsilon$ are the stress and strain differences within the linear region.

It is noted that due to the high sensitivity of the UTM's automatic break detection, the machine-reported fracture strains were triggered prematurely prior to complete physical separation. Therefore, the apparent fracture strain (ε_{app}) was manually calculated based on the final displacement at complete physical separation (L_f) using:

$$\varepsilon_{app} = \frac{L_f - L_0}{L_0} \quad (4)$$

where L_f is the final gauge length at complete physical separation.

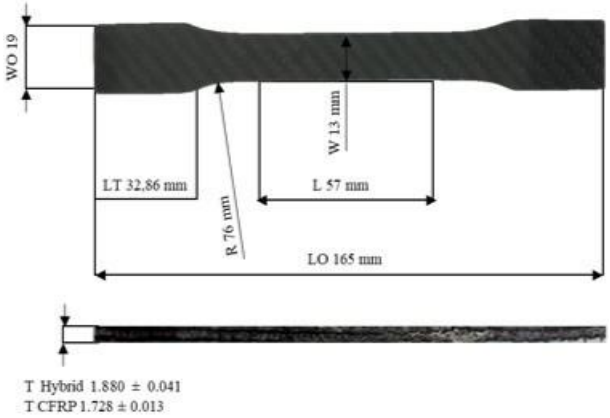


Figure 2. Tensile specimen ASTM D638 Type I.

The reduced-width section and curved transition of the adapted dog-bone geometry may produce a non-uniform stress distribution and local stress concentrations near the gauge-to-fillet transition. Consequently, the measured tensile strengths are interpreted as apparent strengths associated with the specimen geometry employed in this study rather than intrinsic tensile strengths obtained using standard-compliant ASTM D3039 specimens.

2.4.2 Flexural Test

The flexural properties of the hybrid and benchmark CFRP laminates were evaluated using a three-point bending configuration in accordance with ASTM D790. The tests were performed using the Universal Testing Machine (UTM) (TENSILON RTF-2410, A&D Co., Japan) equipped with a 100 kN load cell. Five specimens were tested for each laminate configuration under displacement-controlled loading at a constant crosshead speed of 5 mm/min. A support span of 80 mm was employed. Based on the average specimen thickness, the span-to-thickness ratios were approximately 46.7:1 for CFRP and 41.8:1 for the hybrid laminate. The flexural specimen geometry is illustrated in Figure 3.

 https://doi.org/ 10.25077/metal.10.2.111-123.2026

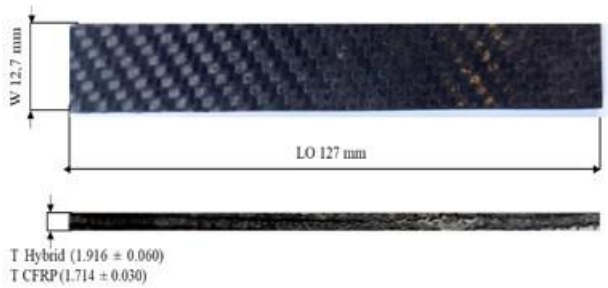


Figure 3. Flexural specimen ASTM D790.

The specimens had an overall length of 127 mm and a nominal width of 12.7 mm. The average thicknesses were approximately 1.7 mm for CFRP and 1.9 mm for the hybrid laminate, reflecting thickness variations associated with the vacuum infusion manufacturing process.

During testing, the applied load and crosshead displacement were continuously recorded until specimen failure. The flexural stress (σ_f) was calculated using the standard formula for three-point bending:

$$\sigma_f = \frac{3PL}{2bT^2} \quad (5)$$

where P is the applied load (in Newtons), L is the support span (in mm), b is the specimen width (in mm), and T is the specimen thickness (in mm). The flexural strain (ε_f) at the outer surface of the specimen was calculated as:

$$\varepsilon_f = \frac{6DT}{L^2} \quad (6)$$

where D is the mid-span deflection (in mm). The flexural modulus (E_f) was derived from the slope of the linear-elastic region of the load–deflection curve using:

$$E_f = \frac{L^3 m}{4bT^3} \quad (7)$$

where m is the slope of the tangent to the initial straight-line portion of the load–deflection curve (in N/mm). The maximum flexural strength, flexural modulus, flexural strain, and flexural stress–strain response were subsequently obtained for further analysis.

2.5 Macroscopic Failure Characterization

Following tensile and flexural testing, the failure characteristics of all specimens were examined through macroscopic visual inspection. Photographs of the fractured specimens were taken from multiple viewing angles (front, rear, and side) to document the overall damage morphology. The observed failure characteristics were subsequently correlated with the corresponding mechanical responses obtained from the tensile stress–strain and flexural stress–strain curves [10].

For the tensile specimens, failure characteristics were evaluated based on fracture location, fracture pattern, and dominant macroscopic damage. The three-character failure mode terminology of ASTM D3039 was used as a descriptive reference to identify and report the observed failure modes. Considering the adapted dog-bone specimen geometry, the assigned codes are presented as descriptive classifications and do not imply full compliance with the standard specimen geometry specified in ASTM D3039. As established in Section 2.4.1, the geometric transition at the fillet radius introduces localized stress concentrations that influence the fracture initiation zone. Accordingly, the failure modes are reported using the ASTM D3039 three-character terminology as descriptive identifiers of the observed failure type, area, and location. These codes describe the macroscopic failure characteristics of the tested specimens and do not imply full compliance with the standard specimen geometry or testing configuration.

For the flexural specimens, macroscopic observations focused on the fracture location, crack initiation, fiber fracture, layer separation, and the overall damage pattern after three-point bending [11]. These observed failure characteristics were then correlated with the mechanical responses to provide a qualitative interpretation of the failure behavior of the hybrid and benchmark CFRP laminates.

3. RESULTS AND DISCUSSION

This section presents the results of the mechanical evaluations and failure mode analysis of the tested specimens. The performance of the [Carbon/Glass/CSM] hybrid laminates was compared against the monolithic CFRP benchmark to evaluate the effects of hybridization on the structural integrity of the material.

3.1. Tensile Performance Analysis

Table 1 shows that the benchmark CFRP exhibited higher tensile strength and elastic modulus than the hybrid laminate. The CFRP achieved a tensile strength of 610.6 MPa and an elastic modulus of 25.8 GPa, compared with 395.7 MPa and 10.4 GPa, respectively, for the hybrid laminate. Uniquely the measured fracture strains did not follow the rule of strength increasing will decreases ductility. It is shown CFRP was broken at 4.7 %GL, while the hybrid laminate at 3.8 %GL.

Table 1. Tensile properties of the benchmark CFRP and hybrid laminates.

Properties	CFRP	Hybrid	Unit
Thickness	1.728 ± 0.013	1.880 ± 0.041	mm
Tensile strength	610.6 ± 56	395.7 ± 41	MPa
Elastic modulus	25.8 ± 3.2	10.4 ± 0.3	GPa
Apparent fracture strain at break	4.7 ± 0.5	3.8 ± 0.5	%GL

Values are expressed as mean ± standard deviation (n = 5).

Figure 4 shows the tensile stress–strain responses of both configurations. The CFRP and the hybrid laminates exhibited an approximately linear-elastic response over most of the loading history, followed by a sudden stress drop immediately after reaching the ultimate tensile strength. No noticeable plastic deformation was observed before fracture, indicating that both laminates retained the characteristic brittle tensile behavior commonly associated with fiber-reinforced polymer composites.

Compared with the benchmark CFRP, the hybrid laminate exhibited a lower stress–strain slope throughout the elastic region, which is consistent with its lower elastic modulus reported in Table 1. Although the hybrid specimens reached lower ultimate tensile stresses, the overall stress–strain profiles remained similar to those of the benchmark CFRP, indicating that the hybridization did not substantially alter the predominantly brittle response of the laminate under tensile loading.

Small stress fluctuations were observed immediately before the ultimate tensile strength in several specimens of both laminate configurations, as indicated by the vibrating curve regions in Figures 4. These fluctuations occurred within a narrow strain interval immediately preceding final fracture and may indicate progressive local damage before catastrophic failure.

However, because the study was limited to macroscopic observations without digital image correlation (DIC) or microscopic characterization techniques such as scanning electron microscopy (SEM), the underlying damage mechanisms responsible for these fluctuations cannot be conclusively identified. Therefore, the observed behavior is interpreted qualitatively and further discussed together with the macroscopic failure observations in Section 3.3.

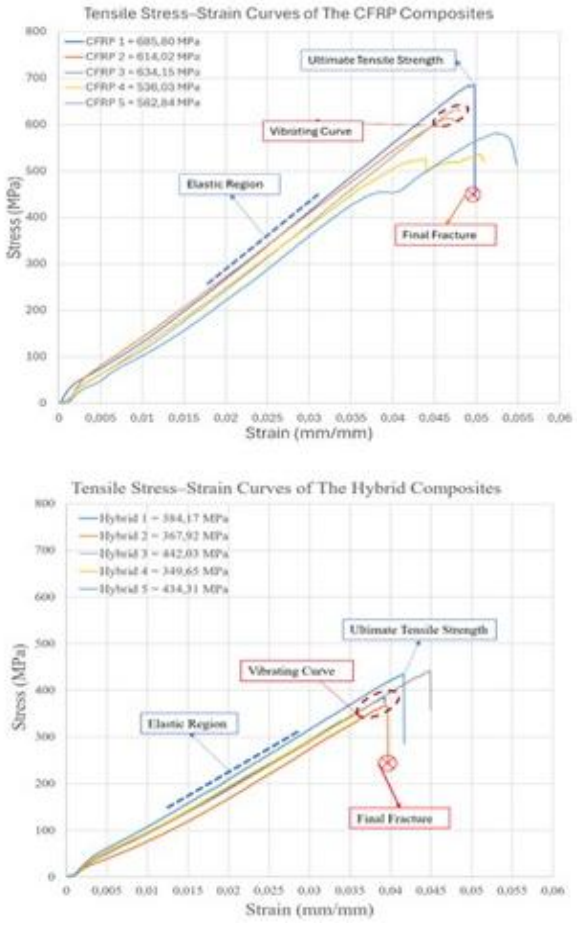


Figure 4. Tensile stress–strain curves: (top) CFRP and (bottom) hybrid laminates.

3.2. Flexural Performance Analysis

Table 2 shows that the CFRP exhibited a higher flexural strength and modulus than the hybrid laminate, with an equal strain at break. The flexural

https://doi.org/ 10.25077/metal.10.2.111-123.2026

strength of CFRP reached 443.9 MPa, while the hybrid laminate was 294.1 MPa. Likewise the average flexural modulus of CFRP was 54.2 GPa, and the hybrid laminate has 32.2 GPa. Both of the configuration was broken at 0.8% of flexural strain.

Table 2. Flexural properties of the benchmark CFRP and hybrid laminates.

Properties	CFRP	Hybrid	Unit
Thickness	1.714 ± 0.030	1.916 ± 0.060	mm
Flexural strength	443.9 ± 17.4	294.1 ± 29.4	MPa
Flexural modulus	54.2 ± 2.4	32.2 ± 2.5	GPa
Flexural strain at break	0.83 ± 0.05	0.85 ± 0.14	%

Values are expressed as mean ± standard deviation (SD), n = 5.

Figure 5 shows the flexural stress–strain responses of both laminate configurations. Prior to reaching the maximum flexural stress, both the benchmark CFRP and the hybrid laminates exhibited an approximately linear-elastic response. Following the peak stress, however, a clear difference in post-peak behavior was observed between the two material systems.

The benchmark CFRP exhibited a relatively abrupt reduction in flexural stress immediately after reaching the maximum load, indicating a predominantly brittle flexural response. Although the specimens retained a residual load-carrying capacity after the initial damage, the post-peak stress decreased rapidly with only limited fluctuations before the final fracture.

In contrast, the hybrid laminates exhibited a more gradual post-peak response characterized by multiple stress fluctuations and extended residual load-carrying regions prior to complete failure. Rather than undergoing a single catastrophic stress drop, several hybrid specimens continued to sustain bending loads after the initial damage, producing a progressive reduction in flexural stress throughout the remaining deformation [12].

The observed post-peak behavior of the hybrid laminates is consistent with the pseudo-ductile characteristics reported for hybrid fiber-reinforced composite laminates, where damage develops progressively and the structure continues to carry load after the initiation of failure [13]. In the present study, this interpretation is supported by the extended post-peak stress response and repeated stress fluctuations observed in the flexural stress–strain curves [14]. Because the characterization was limited to mechanical responses and macroscopic observations, the underlying damage mechanisms cannot be conclusively identified and are therefore discussed qualitatively together with the macroscopic failure observations in Section 3.3.

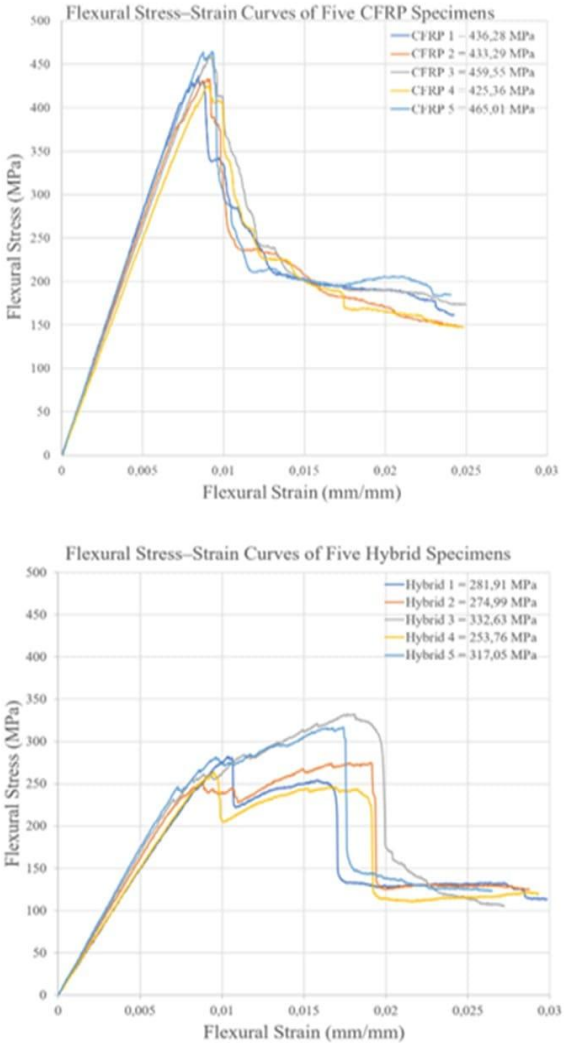


Figure 5. Flexural stress–strain curves: (top) CFRP and (bottom) hybrid laminates.

3.3 Macroscopic Failure Analysis

Macroscopic failure analysis was conducted to correlate the post-test physical damage of both laminate configurations with the mechanical responses discussed in Sections 3.1 and 3.2.

Fractured specimens were visually inspected from multiple orientations (front, rear, side, and localized fracture zones) to identify the dominant damage mechanisms. For the tensile specimens, the observed failure modes were identified using the three-character ASTM D3039 failure mode terminology, with consideration of the adapted dog-bone specimen geometry.

Meanwhile, the flexural specimens were assessed based on macroscopic indicators such as fracture location, crack initiation, interlaminar separation, and permanent deformation patterns. These visual evaluations complemented the mechanical responses observed in the stress–strain curves, particularly the abrupt brittle failure of the CFRP benchmark and the more gradual post-peak flexural response of the hybrid laminates. The detailed findings for the tensile and flexural failures are presented in the following subsections

3.3.1 Tensile Failure Analysis of CFRP and Hybrid Laminates

Figure 6 shows a typical tensile fracture in the hybrid specimen. The fracture initiated within the gauge section near the gauge–fillet transition after the specimen reached its ultimate tensile load. No evidence of grip slippage or grip-induced crushing was observed, indicating that the applied tensile load was effectively transferred into the intended test section.

Macroscopic observation revealed that damage was concentrated within the gauge section, where complete fracture of the carbon fiber bundles was accompanied by local matrix fragmentation. The woven architecture outside the fractured region remained largely intact, indicating that catastrophic failure was localized and did not propagate throughout the gauge length. Limited matrix fragmentation developed adjacent to the fracture surface, whereas the surrounding laminate maintained its structural continuity.



Figure 6. Magnified views of the localized fracture region in the representative hybrid specimen: (left) front view; (right) rear view.

Figure 7 shows that damage remained localized around the fracture region through the laminate thickness. Carbon fiber fracture governed the ultimate failure of the laminate, whereas fiber pull-out, fiber bridging, limited edge delamination, and matrix fragmentation developed as secondary damage mechanisms.

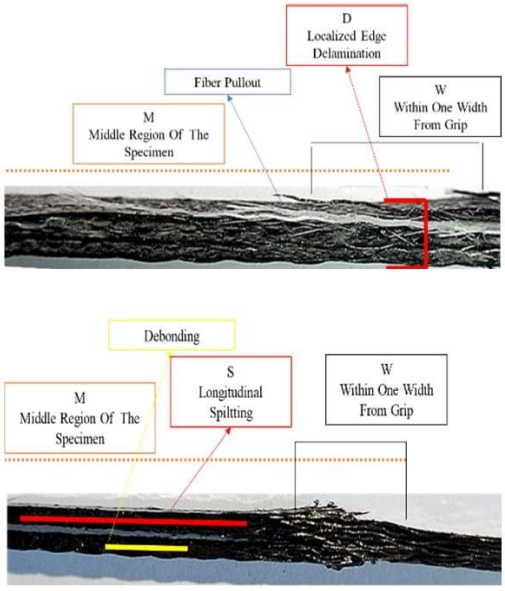


Figure 7. Side-view of the through-thickness fracture tensile specimens: (left) CFRP, (right) the hybrid laminate.

A complete rupture of the carbon fiber bundles that accompanied by a localized matrix fragmentation and a limited edge delamination adjacent to the fractured cross-section. Fiber pull-out and fiber bridging were also observed, indicating that

https://doi.org/ 10.25077/metal.10.2.111-123.2026

portions of the glass-fiber reinforcement remained continuous after carbon fiber rupture. No extensive interlaminar delamination or progressive longitudinal crack propagation was observed along the gauge length.

The observed tensile failure modes were identified using the three-character coding terminology of ASTM D3039 [15]. The first character denotes the failure type, the second indicates the failure area, and the third specifies the failure location. The assigned failure codes for both laminate configurations are presented in Figure 8.



Figure 8. Descriptive identification of tensile failure modes using ASTM D3039 terminology: (a) CFRP and (b) hybrid laminate specimens.

As shown in Figure 8, the CFRP specimens exhibited three SWM failure modes (specimens 1–3), one GIB failure mode (specimen 4), and one GIT failure mode (specimen 5). In contrast, all five hybrid specimens exhibited DWM failure modes. The corresponding descriptions of these failure codes are provided in Table 3.

Table 3. Descriptions of failure mode codes based on ASTM D3039 terminology.

Code	Meaning
DWM	Edge delamination – Within one width from grip – Middle
SWM	Longitudinal splitting – Within one width from grip – Middle
GIB	Grip/Tab – Inside grip – Bottom
GIT	Grip/Tab – Inside grip – Top

DWM indicating localized edge delamination occurring within one specimen width from the grip and extending through the middle region of the specimen. Although fracture initiated near the gauge–fillet transition because of the geometry, all specimens exhibited consistent macroscopic failure characteristics without extensive interlaminar crack propagation.

3.3.2 Flexural Failure Analysis of Hybrid and CFRP Laminates

Macroscopic examination of the flexural specimens revealed a distinct contrast in failure behavior between the benchmark CFRP and the Carbon/Glass/CSM hybrid laminates. While both configurations experienced failure initiated at the tensile side (bottom surface) beneath the loading nose, the most striking physical difference lies in the post-failure deformation state.

Figure 9 presents the representative hybrid specimen immediately after flexural failure while still under bending conditions in the testing machine.

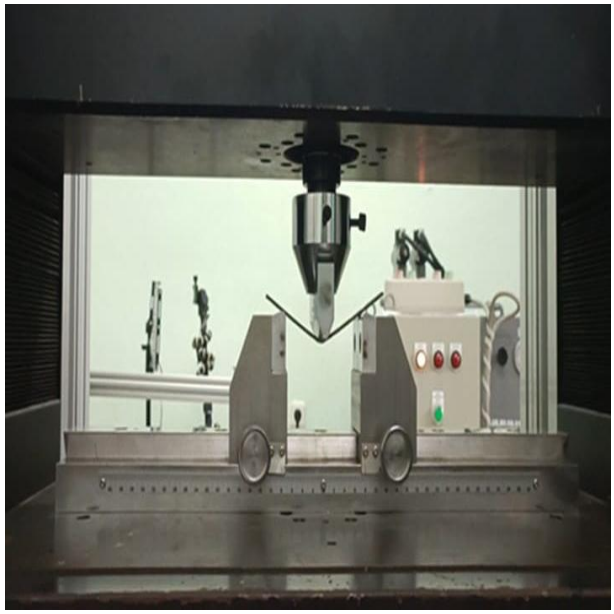


Figure 9. Representative hybrid flexural specimen in the testing machine.

In addition to the differences observed in the flexural stress–strain responses, a distinct spring-back phenomenon was identified after unloading the specimens from the three-point bending test [16]. The post-test deformation state of the specimens provides complementary macroscopic evidence of the different flexural failure behaviors exhibited by the hybrid and benchmark CFRP laminates.

Figure 10 shows that the hybrid specimens retained a relatively straight shape after unloading, indicating a visible spring-back response. In contrast, the CFRP specimens exhibited brittle fracture and retained permanent bending deformation.



1 2 3 4 5 1 2 3 4 5

(a) (b)

Figure 10. Side-view flexural specimen, (left) the CFRP, (right) the hybrid.

This macroscopic difference is quantitatively corroborated by the flexural stress-strain responses presented in Figures 11 alongside the experimental data representative in the test records. Figure 11 shows that after reaching the maximum load, the CFRP specimens suffered an abrupt post-peak stress drop with minimal load retention. This sharp decline indicates a brittle failure mode dominated by the immediate fracture of the outer carbon fiber skins, leaving no reinforcing mechanism to sustain further deformation, thus preventing any spring-back effect.

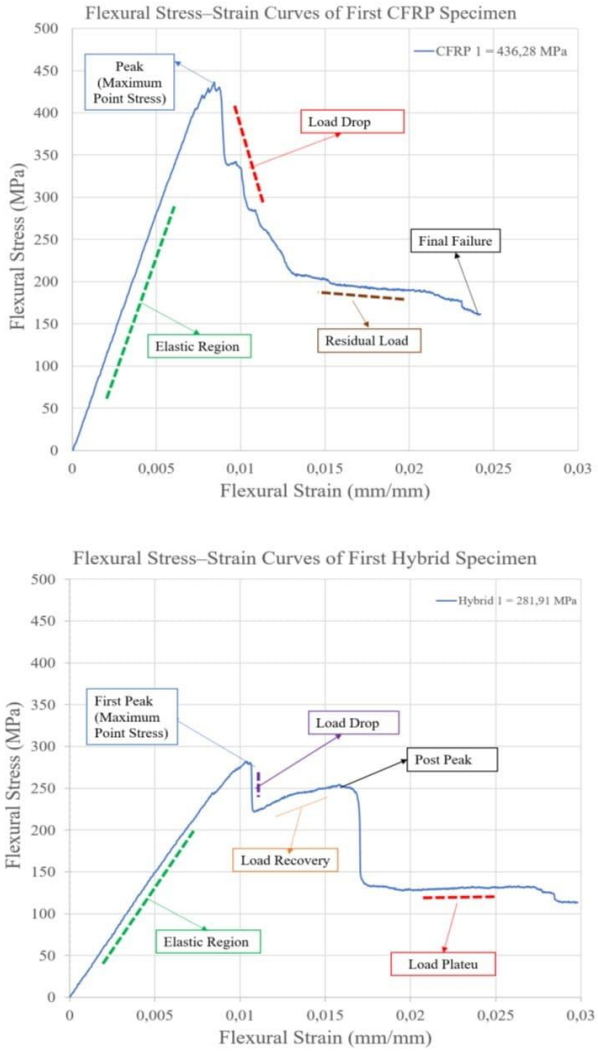


Figure 11. Flexural stress–strain responses during testing: (top) CFRP and (bottom) hybrid laminates.

Figure 11 also shows that the hybrid laminate has a second peak. Following the initial peak, the stress-strain curves of the hybrid specimens display a distinctive sawtooth pattern, characterized by repeated local stress fluctuations and an extended load plateau. This gradual, progressive post-peak stress reduction allows the laminate to maintain structural integrity and carry residual loads over a larger strain interval before final fracture [17]. The data recorded in the flexural test tables indicate that the hybrid laminate sustains this deformation without immediate catastrophic failure.

 https://doi.org/ 10.25077/metal.10.2.111-123.2026

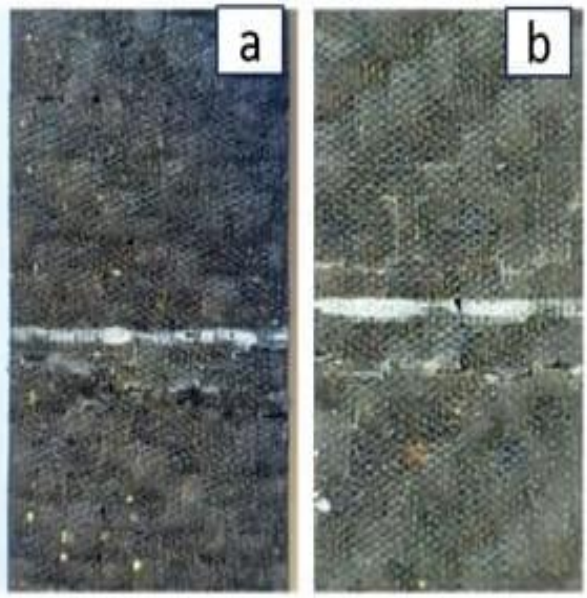


Figure 12. Macroscopic appearance of the localized flexural fracture region: (a) CFRP and (b) hybrid laminate.

The difference in failure behavior is further highlighted by comparing the localized fracture morphology of the specimens, as presented in Figure 12. Macroscopically, the monolithic CFRP specimen (Figure 12a) exhibits a sharper, fully propagated transverse fracture accompanied by visible matrix debonding, which corresponds to the abrupt, brittle release of stored strain energy observed in its stress-strain curve. Conversely, the hybrid specimen (Figure 12b) shows a clean transverse crack at the mid-span with minimal lateral spreading, suggesting that local fiber rupture occurred without generating extensive delamination.

3.4. Implications for Lightweight UAV Structures

To evaluate the structural feasibility of the proposed hybrid laminate for UAV applications, its mechanical performance was benchmarked against recent findings in composite material characterization for aerospace structures. Additively manufactured composite materials for multirotor UAV airframe parts have been investigated, and continuous fiber fabrication (CFF) with fiberglass reinforcement achieved a maximum tensile strength of up to 164 MPa [18]. In contrast, the hybrid laminate in the present study achieved a tensile strength of 395.6 MPa, which is more than double the maximum capacity of those printed composites.

Furthermore, an optimized bamboo-carbon hybrid composite for UAV wing spars exhibited a flexural strength of 288.5 MPa and a flexural modulus of 31.8 GPa [19]. Notably, the hybrid laminate developed in this study achieved a flexural strength of 294.1 MPa and a flexural modulus of 32.2 GPa—values that slightly exceed the optimized bamboo-carbon hybrid composite. Likewise, CFRP/ABS/CFRP sandwich structures fabricated via fused deposition modeling (FDM) achieved a tensile strength of up to 93.3 MPa and a Young's modulus of 10.1 GPa [20]. In comparison, the proposed vacuum-infused hybrid laminate achieves a significantly higher tensile strength (395.6 MPa) and elastic modulus (10.40 GPa), indicating that the vacuum-infusion process combined with the [C/G/CSM/C/G/CSM/C] stacking sequence offers superior mechanical performance for load-bearing UAV components.

Regarding the influence of fiber arrangement, balanced cross-ply and quasi-isotropic C/GFRP hybrids have been characterized, where the positioning of GFRP layers in the transverse direction significantly enhanced the tensile modulus, while the inclusion of ± 45° CFRP layers improved flexural strength through better shear stress distribution [21]. The strategic stacking of outer carbon layers and inner glass/CSM core layers in this study similarly promoted a progressive failure mode, which aligns with the overarching review on hybrid carbon/glass fiber reinforced polymers, emphasizing that the synergy between high-modulus carbon fibers and high-strain glass fibers can significantly improve damage tolerance without excessive cost [22].

In summary, the mechanical properties of the proposed hybrid laminate fall well within the acceptable range for secondary UAV structural components, particularly when compared to optimized hybrid composites for wing spars [18], [19] and other additively manufactured airframe

parts [20]. The observed progressive post-peak flexural response and visible spring-back after unloading may be relevant to lightweight secondary UAV structures where residual load-carrying capacity is desirable.

However, the present study was limited to mechanical testing and macroscopic visual inspection; SEM fractography and DIC analysis were not performed. Therefore, the underlying damage mechanisms and strain-field evolution cannot be established from the available evidence. Accordingly, the observed behavior is described as a progressive post-peak flexural response rather than being classified as pseudo-ductile behavior.

4. CONCLUSION

Based on the experimental investigation, the following conclusions can be drawn:

a. The vacuum-infused Carbon/Glass/CSM hybrid laminate exhibited a lower tensile and flexural strengths than the CFRP laminate.
b. The hybrid laminate showed a better-balanced structural performance under bending.
c. The CFRP demonstrated tensile and flexural has a predominantly brittle failure characterized by abrupt post-peak stress reduction.
d. The hybrid laminate exhibited a more gradual post-peak flexural response, characterized by repeated stress fluctuations and residual load-carrying capacity before final failure.
e. The hybrid laminate showed a visible spring-back response after the bending load was released, with the specimens retaining a relatively straight shape, whereas the CFRP specimens retained permanent bending deformation.
f. The CFRP were predominantly broken in SWM mode, while the hybrid laminates were always in DWM mode.
g. Overall, the proposed vacuum-infused hybrid laminate demonstrates potential for a lightweight structural applications requiring a balance between stiffness, progressive post-peak flexural response, and progressive failure behavior. These characteristics make the laminate a promising alternative for secondary UAV structural components, where controlled damage progression and residual structural integrity are desirable in addition to mechanical performance.

REFERENCES

[1] C. Lytridis *et al.*, "An Overview of Cooperative Robotics in Agriculture," *Agronomy*, p., 2021, doi: 10.3390/agronomy11091818.

[2] A. Nebrida, "Smart integration in agriculture: an Arduino-driven rice grain dryer for optimal post-harvest management," *Journal of Electrical Systems and Information Technology*, vol. 11, p., 2024, doi: 10.1186/s43067-024-00170-0.

[3] S. Masiado *et al.*, "GrainBot: An Android-Controlled Rice Grain Collector Robot," *International Journal of Advanced Science Computing and Engineering*, p., 2025, doi: 10.62527/ijasce.7.2.258.

[4] J. Tuanama-Aguilar *et al.*, "Construction of an Automated Removal Robot for the Natural Drying of Cacao Beans," *Sensors (Basel)*, vol. 25, p., 2025, doi: 10.3390/s25051520.

[5] A. Chand *et al.*, "Design and Analysis of Photovoltaic Powered Battery-Operated Computer Vision-Based Multi-Purpose Smart Farming Robot," *Agronomy*, p., 2021, doi: 10.3390/agronomy11030530.

[6] A. Ghobadpour, A. Cárdenas, G. Monsalve, and H. Mousazadeh, "Optimal Design of Energy Sources for a Photovoltaic/Fuel Cell Extended-Range Agricultural Mobile Robot," *Robotics*, vol. 12, p. 13, 2023, doi: 10.3390/robotics12010013.

[7] S. Patted, K. K, K. B. D, and S. R, "Solar Powered Automated Multitasking Agricultural Robot," *IJIREEICE*, p., 2024, doi: 10.17148/ijireeice.2024.12423.

[8] [8] K. Luo, Y. Chen, R. Lin, C. Liang, and Q. Zhang, "A Portable Agriculture Environmental Sensor with a Photovoltaic Power Supply and Dynamic Active Sleep Scheme," *Electronics (Basel).*, p., 2024, doi: 10.3390/electronics13132606.

[9] C. Xu, Y. Song, M. Han, and H. Zhang, "Portable and wearable self-powered systems based on emerging energy harvesting technology," *Microsyst. Nanoeng.*, vol. 7, p., 2021, doi: 10.1038/s41378-021-00248-z.

[10] M. A. Z. Abidin, M. Mahyuddin, and M. A. A. M. Zainuri, "Solar Photovoltaic Architecture and Agronomic Management in

Agrivoltaic System: A Review," *Sustainability*, p., 2021, doi: 10.3390/su13147846.

[11] S. Ghasemi and I. Sadeghkhani, "Toward Sustainable Energy-Agriculture Synergies: A Review of Agrivoltaics Systems for Modern Farming Practices," *Solar RRL*, vol. 9, p., 2025, doi: 10.1002/solr.202500041.

[12] A. Chairany, R. Buaton, and R. Puspadini, "Penerapan Internet of Things pada Mekanik Prototipe Robot Pengaduk Gabah," *Repeater : Publikasi Teknik Informatika dan Jaringan*, p., 2025, doi: 10.62951/repeater.v3i3.617.

[13] I. Habriansyah *et al.*, "Kontrol Sistem Mekanik Prototipe Robot Pengaduk Gabah Berbasis Internet of Things," *Jurnal Teknik Mesin Sinergi*, p., 2023, doi: 10.31963/sinergi.v21i1.4222.

[14] A. Saswito, M. Musfirayanti, R. Tandioga, and I. Habriansyah, "Pengembangan Prototipe Robot Pengaduk Menggunakan Sensor Suhu dan Kelembaban untuk Memantau Tingkat Kekeringan Gabah Berbasis Internet of Things," *Jurnal Teknik Mesin Sinergi*, p., 2022, doi: 10.31963/sinergi.v20i1.3483.

[15] M. R. Putri, F. Setyawan, and S. Sumadi, "Sistem Kontrol Beban Dan Monitoring Daya Baterai Pada Panel Surya 50wp Untuk Aplikasi Penerangan Berbasis Internet Of Things," *Jurnal Informatika dan Teknik Elektro Terapan*, p., 2022, doi: 10.23960/jitet.v10i3.2640.

[16] A. Sifa, "Rancang Bangun Pembangkit Tenaga Surya (Plts) 200wp Untuk Suplai Daya Sistem Kendali Dan Monitoring Pemeliharaan Tanaman Media Air," *Orbith: Majalah Ilmiah Pengembangan Rekayasa dan Sosial*, p., 2023, doi: 10.32497/orbith.v19i2.5002.

[17] M. Syahwil and N. Kadir, "Rancang Bangun Modul Pembangkit Listrik Tenaga Surya (PLTS) Sistem Off-grid Sebagai Alat Penunjang Praktikum Di Laboratorium," *Jurnal Pengelolaan Laboratorium Pendidikan*, p., 2021, doi: 10.14710/jplp.3.1.26-35.

[18] M. K. S. Al-Ghezi, R. Ahmed, and M. Chaichan, "The Influence of Temperature and Irradiance on Performance of the photovoltaic panel in the Middle of Iraq," *International Journal of Renewable Energy Development*, p., 2022, doi: 10.14710/ijred.2022.43713.

[19] O. Bamisile, C. Acen, D. Cai, Q. Huang, and I. Staffell, "The environmental factors affecting solar photovoltaic output," *Renewable and Sustainable Energy Reviews*, p., 2025, doi: 10.1016/j.rser.2024.115073.

[20] S. Chtita, A. Derouich, E. Ghzizal, and S. Motahhir, "An improved control strategy for charging solar batteries in off-grid photovoltaic systems," *Solar Energy*, vol. 220, pp. 927–941, 2021, doi: 10.1016/j.solener.2021.04.003.

[21] A. Bala, M. B. Alao, A. O. Oyedun, O. O. Alabi, and M. Adamu, "Performance Evaluation of a Solar Photovoltaic (PV) Module at Different Solar Irradiance," *International Journal of Engineering and Applied Sciences*, p., 2024, doi: 10.24107/ijeas.1430556.

[22] E. S. Ward, N. Gad, L. Rabeh, and A. Yahia, "Effects of Solar Irradiance and Temperature on Photovoltaic Module Characteristics using a capacitive load method," *Menoufia Journal of Electronic Engineering Research*, p., 2023, doi: 10.21608/mjeer.2023.283915.

[23] S. N. M. Sabudin and N. M. Jamil, "Mathematical model for predicting the performance of photovoltaic system with delayed solar irradiance," *Kuwait Journal of Science*, p., 2024, doi: 10.1016/j.kjs.2024.100207.